Fast microwave-assisted solvothermal synthesis of metal nanoparticles (Pd, Ni, Sn) supported on sulfonated MWCNTs: Pd-based bimetallic catalysts for ethanol oxidation in alkaline medium

Tendamudzimu Ramulifho[a,b], Kenneth I. Ozoemena*[,a,b,1],
Remegia M. Modibedi[a,1], Charl J. Jafta[a], and Mkhulu K.
Mathe[a,1]

[a.] *Energy and Processes Unit, Materials Science and Manufacturing, Council for Scientific and Industrial Research (CSIR), Pretoria 0001, South Africa.*

[b.] *Department of Chemistry, University of Pretoria, Pretoria 0002, South Africa.*

*Author to whom correspondence should be addressed: (K.I. Ozoemena):
Tel.:+27128413664; Fax: +27128412135; E-mail address:
kozoemena@csir.co.za

[1] Active ISE member

Abstract

The preparation of metal nanoparticles (Pd, Ni, Sn) supported on sulfonated multi-walled carbon nanotubes (SF-MWCNTs) using a very rapid microwave-assisted solvothermal strategy has been described. Electrocatalytic behavior of the SF-MWCNT-Pd and its 'mixed' bimetallic electrocatalysts (i.e., SF-MWCNT-PdSn$_{mix}$ and SF-MWCNT-PdNi$_{mix}$) towards ethanol oxidation in alkaline medium was investigated. The result shows that the mixed Pd-based catalysts (obtained by simple ultrasonic-mixing of the individual MWCNT-metal nanocomposites) gave better electrocatalytic activity than their alloy nanoparticles (obtained by co-reduction of metal salts) or Pd alone. The SF-MWCNT platform gave better electrocatalytic performance compared to the unsulfonated and commercial Vulcan carbons. Detailed electrochemical studies (involving cyclic voltammetry, chronoamperometry, chronopotentiometry, and impedance spectroscopy) prove that the electrocatalytic oxidation of ethanol at the SF-MWCNT-PdNi$_{mix}$ platform is more stable, occurs at lower potential, gives lower Tafel slopes, with faster charge-transfer kinetics compared to its SF-MWCNT-PdSn$_{mix}$ counterpart. Also, result revealed that SF-MWCNT-PdNi$_{mix}$ is more tolerant to CO poisoning than the SF-MWCNT-PdSn$_{mix}$. The results provide some important insights into the electrochemical response of microwave-synthesised Pd-based bimetallic catalysts for potential application in direct ethanol alkaline fuel cell technology.

1.   Introduction

Direct alcohols alkaline fuel cells (DAAFCs) are electrochemical devices that convert chemical energy stored in liquid alcohols into electricity operating in alkaline medium [1-3]. The commercialization of direct alcohol fuel cells has been limited due to the use of the platinum catalyst which is expensive. Palladium (Pd)-based electrocatalysts have begun to attract intense research interest in DAAFCs as attractive potential replacement for the current platinum (Pt)-based electrocatalysts. This is mainly because Pd is more abundant in nature than Pt, and exhibits unique electrocatalytic properties towards alcohol oxidation in alkaline media [4].

Support materials play an important role on the performance of electrocatalysts for fuel cells. Different materials that have been studied as electrocatalysts' supports include carbon nanotubes (CNTs) [5-11] carbon blacks [12], carbon microspheres [13], tungsten carbides [14-16], carbon nanofibers [17] and TiO_2 nanotubes [18]. Indeed, due to their high mechanical strength, excellent conductivity, and high surface areas, CNTs are

3

increasingly becoming attractive supports for electrocatalysts for electrochemical energy storage and conversion systems [19-21]. However, for the CNTs to be effectively used as support materials, they need to be functionalized to enhance their dispersibility in solvents, and to permit anchorage of the metal. Some notable methods of functionalizing CNTs include acid treatments [22, 23] and sulfonation processes [24, 25].

The methods used in preparing electrocatalysts have great influence on the structure, size, morphology, and hence the catalytic properties of the catalysts. The microwave-assisted solvothermal synthesis (MWAS) is an attractive synthetic strategy for the preparation of nanosized catalysts [26-28]. It is faster, cleaner, simpler than the conventional borohydride reduction methods [26-28]. For example, Manthiram and co-workers [28] recently reported that alloys, synthesised by the MWAS strategy, enhanced electrocatalytic reduction of oxygen compared to their counterparts synthesised by the conventional borohydride reduction method.

This study reports the preparation of metal nanoparticles (Pd, Ni, Sn) supported on sulfonate-functionalized multi-walled carbon nanotubes (SF-MWCNTs) using the fast MWAS approach within a very short reaction time at temperatures as low as 170 °C without the need for post-synthesis heat treatments. We also prove that the PdM nanocomposite mixtures (obtained by ultrasonic-mixing of the

4

individual Pd and Ni or Sn) rather than their bimetallic nanoalloys (obtained by co-reduction process) can serve as efficient electrocatalysts for the oxidation of ethanol in alkaline medium. Our result clearly reveals from voltammetric and impedance data that these SF-MWCNT-PdM nanocomposites exhibit an appreciable level of tolerance to carbon monoxide (CO) poisoning during ethanol oxidation.

2.   Experimental

2.1 Materials and reagents

Absolute ethanol (C_2H_5OH, ACS reagent grade), multi-walled carbon nanotubes ($\geq$ 95% as MWCNT, O.D $\times$ I.D $\times$ length, 7-15 nm $\times$ 3-6 nm $\times$ 0.5 – 200 μm), hydrogen peroxide (H_2O_2, 30 % by weight), Nafion perfluorinated ion-exchange resin (5 wt% in mixture of lower aliphatic alcohols), potassium hydroxide pellets (KOH, ACS reagent, > 85% pure), Sulfuric acid (H_2SO_4, 95 – 97 % pure), tin (II) chloride dehydrate ($SnCl_2$. $2H_2O$, 99.995%) were obtained from Sigma-Aldrich. Acetic anhydride ((CH_3-CO)$_2$O, ACS reagent grade), ethylene glycol ($OHCH_2CH_2OH$, extra pure), and nitric acid (HNO_3, 65% extra pure) were obtained from Merck. Hydrophilic polypropylene membrane filters 47 mm in diameter, 0.2 μm pore size were obtained from Pall Corporation. Nickel chloride ($NiCl_2$, 60 mesh 99.5%) pure was obtained from Cerac Incorporated. Palladium (II) chloride ($PdCl_2$) was obtained from South Africa

Precious Metal. Carbon black (Vulcan XC-72 was supplied by Cabot Corporation, MA, USA. Pure nitrogen and carbon monoxide (CO) were supplied by Air Liquide (Pty) Ltd (South Africa). Ultra pure water (resistivity: 18.2 MΩcm) was obtained from a Milli-Q water system (Millipore Corp., Bedford, MA, USA). All other reagents were of analytical grade and were used as received from the suppliers without further purification.

2.1.1 Sulfonate-functionalization of MWCNTs

The pristine MWCNTs were first purified and COO-functionalized as described previously [22, 23]. Briefly, 1 g of MWCNTs was added to 140 mL of 2.6 M HNO_3, and the mixture was refluxed for 24 h. The carbon nanotube sediments were separated from the reaction mixture, washed with distilled water, and sonicated in a concentrated H_2SO_4 / HNO_3 mixture (3:1 ratio) for 24 h. The sediment was thereafter washed with distilled water, stirred for 30 min in a 4:1 H_2SO_4 / H_2O_2 mixture (4:1 ratio) at 70 ° C, and then washed again with ultrapure water. The purified, acid-functionalized MWCNT slurry was then oven-dried at 110 °C overnight to obtain the solid black product (herein abbreviated as AF-MWCNTs).

The AF-MWCNTs (containing oxo-functional groups, mainly – COOH) were sulfonated following the method described elsewhere [25]. In brief, 120 mg of the purified MWCNTs was added to a mixture of 20 mL H_2SO_4 and 300 mL of acetic anhydride holding

continuous stirring at 70 °C for 2 h. After 2 h, the reaction mixture was allowed to cool, continuously stirred until room temperature. The resulting product (abbreviated herein as SF-MWCNT) was repeatedly washed with ultrapure water and dried at 70 °C overnight in an oven.

2.1.2 Preparation of SF-MWCNT-nanoM (M = Pd, Ni, Sn)

The metal (Pd, Ni and Sn) nanoparticle catalysts were supported onto the walls of the SF-MWCNTs by adopting the microwave polyol process as reported in the literature [29], summarised in scheme 1. In brief, 3.0 mL of 0.05 M aqueous $PdCl_2$ solution and 50 mL of EG were introduced into a 250 ml Erlenmeyer flask. The synthesis solution pH was adjusted to ~ 7.4 by using 0.8 M aqueous KOH solution. 80 mg of SF-MWCNTs was then added into the above solution and ultrasonically dispersed in the solution for 1 h. The solution was then transferred into a liner-rotor 16 F100 TFM vessel, then placed in a microwave (Multiwave 3000 sample preparation system, 1400 Watts, Anton Paar) and heated using 1000 Watts at 170 °C for 60 s. The time taken to reach 170 °C was about 13 min, and then the microwave was stopped, allowed to cool before the reaction vessel can be removed. Within 120–170 °C range, EG is believed to generate the reducing species for the reduction of the metal ions to metallic particles at high temperatures, so it is possible that metal reduction process occurred within the 13 min

reaction time. The resulting suspension was separated by filtration and the obtained residue washed with acetone and ultra pure water. The final solid product (abbreviated herein as SF-MWCNT-Pd) was dried at 110 °C overnight in an oven. The SF-MWCNT-Sn and SF-MWCNT-Ni were prepared using a similar procedure to the SF-MWCNT-Pd using $SnCl_2$ and $NiCl_2$ precursors, respectively. To compare the substrate effect of differing carbon support materials, Pd nanoparticles were also supported onto Vulcan XC-72 (Vulcan-Pd) and AF-MWCNT (AF-MWCNT-Pd). Also, for comparison, Pd-M nano-alloys (i.e., PdNi and PdSn, obtained by co-reduction and supported on SF-MWCNTs) were studied, abbreviated herein as SF-MWCNT-PdNi and SF-MWCNT-PdSn. The ratios of Pd, Sn or Ni were controlled by stoichiometric calculation and confirmed by energy dispersive X-ray spectroscopy (EDX) measurements.

2.2   Instruments and Procedures

The transmission electron microscope (TEM) micrographs were obtained using a JEOL 2010 TEM system operating at 200 kV. The TEM samples were prepared by ultrasonicating a dispersion of the carbon-supported catalysts in ethanol. A drop of the suspension was cast onto the carbon film covered Cu grid for analysis. The X-ray diffraction (XRD) patterns of the catalysts were obtained using an X-ray diffractometer (XRD, SCINTAG-XDS 2000) with Cu Kα radiation source, λ=1.5418 Å operating at 40 kV and 200 mA. The

XRD diffractograms were obtained in a scan range between 0 and 90°. Fourier-transform infrared (FTIR) spectra were recorded using Spectrum 100 FTIR spectrometer (Perkin Elmer). The energy dispersive x-ray spectra (EDX) were obtained from NORAN VANTAGE (USA). X-ray photoelectron spectroscopy (XPS) experiments were carried out on a Kratos Axis Ultra-DLD system (Shimadzu) with Mg Kα radiation (hυ = 1253.6 eV). Binding energies were calibrated using the containment carbon (C1s = 284.6 eV). All electrochemical experiments were carried out at room temperature with a standard three-electrode cell using an Autolab potentiostat PGSTAT 302N (Eco Chemie, Utrecht, Netherlands) driven by the General Purpose Electrochemical Systems data processing software (GPES and FRA softwares version 4.9). The working electrode was a modified glassy carbon disk electrode (GCE, Bioanalytical systems, diameter = 3.0 mm). A Pt rod and Ag|AgCl, saturated 3 M KCl) were used as a counter and reference electrode, respectively. Electrochemical impedance spectroscopy (EIS) measurements were performed with Autolab Frequency Response Analyser (FRA) software between 100 kHz and 10 mHz with the amplitude (rms value) of the ac signal of 10 mV. All solutions were de-aerated by bubbling pure nitrogen prior to each electrochemical experiment.

2.2.1 Electrode modification process

2 mg carbon material (AF-MWCNTs or SF-MWCNTs or Vulcan XC-72) with or without Pd or Pd-M nanoparticles or nano-alloy was thoroughly dispersed in 2 ml ethanol and 100 µL 5wt % Nafion® solution with the aid of ultrasonic stirring (Bransonic 52 bath). To allow for proper mixing, each mixture was allowed to stay overnight after preparation before carrying out further experiment. A GCE was polished to a mirror finish with alumina slurry (nano powder, Aldrich) and then cleaned by ultrasonic stirring in acetone and deionised water for 3 min respectively. 10 µL of the mixture (pre-sonicated again for about 1 min) was then cast onto the surface of the cleaned GCE. The electrode was then dried at 80 °C in an oven. The following electrodes were studied: GCE modified with (a) SF-MWCNTs containing Pd alone (abbreviated as SF-MWCNT-Pd), (b) mixtures of SF-MWCNTs containing Pd and Ni (abbreviated as AF-MWCNT-PdNi$_{mix}$), and (c) mixtures of SF-MWCNTs containing Pd and Sn (abbreviated as AF-MWCNT-PdSn$_{mix}$). For comparison with the Pd-M$_{mix}$, the electrocatalysis of Pd-M alloys (abbreviated as AF-MWCNT-PdNi and AF-MWCNT-PdSn) were studied using cyclic voltammetry (CV) only. The Pd loading of each electrode was maintained at 6.7 µg.

2.2.2 CO-stripping measurements

0.5 M KOH electrolyte solution was purged by bubbling gaseous nitrogen for 15 min to remove dissolved oxygen. The adsorption of

CO was achieved by purging the KOH electrolyte solution with gaseous carbon monoxide for 30 min while keeping the electrode potential at -0.2 V vs. Ag|AgCl (sat. KCl). After the adsorption of CO monolayer, gaseous nitrogen was vigorously bubbled into the solution to remove traces of dissolved CO.

3.   Results and discussion

3.1   Significance of the microwave synthetic method

Scheme 1 summarises the synthetic process adopted in this work. To our knowledge, this is the first instance microwave-assisted synthetic strategy has been employed to support Pd, Ni and Sn nanoparticles onto sulfonate-functionalized MWCNTs. Microwave method is highly advantageous over the conventional borohydride reduction methods; the reaction mechanism of microwave methodology is described elsewhere [28,30]. The MWAS method provides a uniform nucleation environment and offers highly crystalline monodispersed metal nanoparticles. In this method, ethylene glycol (EG) was used as the solvent, as it can be rapidly heated by microwave radiation, provides the reducing environment for the reaction to prevent the oxidation of the metal catalysts, acts as a stabiliser, limiting particle growth, and prohibiting agglomeration. The metal ions coordinate with the functional groups (i.e., $-COOH$, $-C=O$, and $-SO_3H$) on the MWCNTs, functioning as a nucleation precursors that are finally reduced to produce metal

nanoparticles on the MWCNTs. The pH of the synthesis solution greatly influences the stability and size of metal particles. EG is believed to be oxidized to acetic acid at high pH which then acts as a stabilizer. Thus, in this work, the synthesis pH was increased to ~7.4 as reported by Zhao *et al*. [31].

3.2 *Spectroscopic and microscopic characterisation*

Figure 1 compares XRD patterns of the SF-MWCNT-Pd, SF-MWCNT-Ni, SF-MWCNT-Sn, SF-MWCNT-PdNi$_{mix}$, and SF-MWCNT-PdSn$_{mix}$. The featured XRD peaks of Pd, Sn and Ni crystals clearly indicate that these metal particles were successfully reduced and supported onto the SF-MWCNTs surface. The diffraction peaks of the Pd are very well defined and can be indexed to (111), (200), and (220) reflections of a palladium face-centred cubic (fcc) crystal structure (JCPDS card No. 88-2335). The intensity ratio of the crystal planes (111):(200):(220) is 4:2:1. Unlike the Pd, the diffraction peaks for the Ni (JCPDS card No. 88-2326) and Sn (JCPDS card No. 65-7657) are weak, suggesting amorphous structures. The average crystallite size for the Pd (111), using the Debye-Scherrer equation, was about 30 nm. The catalyst particles are agglomerated on the nanotubes as seen on the TEM images. Using the conventional borohydride-assisted method, however, Sun *et al.* [25] had observed a more uniform dispersion of the Pd catalyst on the S-MWCNTs and smaller particle size of 4.5 nm. It appears that our microwave-assisted

method leads to large-sized nanoparticles due to agglomeration of catalyst particles on the MWCNTs support. As also seen in Figure 1, the signature peak of Pd in the 'mixed' catalysts are shifted to higher 2θ values compared to the corresponding peak in the SF-MWCNT-Pd, which is an indication of the formation of alloy and contraction of the Pd–Pd interatomic distance [32].

Figure 2 shows typical TEM images of the (a) SF-MWCNTs with inset of pristine MWCNTs, (b) SF-MWCNT-Pd, (c) SF-MWCNT-Ni, and (d) SF-MWCNT-Sn nanocomposites. As expected, the acid-treated and functionalized MWCNTs exhibit more defects than its pristine counterpart. The images show that the metal catalysts appear as agglomerates onto the walls of the SF-MWCNTs. From the comparative EDX profiles of the SF-MWCNT-Pd, SF-MWCNT-Sn, and SF-MWCNT-Ni nanocomposites (Figure 3) the weight content of each of the three metals was 24.61±0.3% for Pd, 25.13±0.26 % for Sn, and 16.01±0.21 % for Ni. These values are in the expected range for the synthesis, indicating satisfactory synthetic strategy. The slight deviations in values may be related to the loss of the support and/or the metal catalyst during the synthesis. The presence of oxygen peaks on all the EDX spectra arise from the MWCNTs, the sulphur peaks suggest the sulfonic acid groups. The occurrence of Cl peaks is attributed to the impurity from the precursor chloride salts used during the synthesis.

Figure 4a shows detailed XPS of the SF-MWCNT-PdNi$_{mix}$, showing the signature doublet consisting of a high-energy peak (Pd 3d$_{3/2}$) and a low-energy peak (Pd 3d$_{5/2}$). The spectrum is deconvoluted into six peaks representing the Pd 3d and the PdO$_x$ peaks. The Pd 3d$_{5/2}$ peak of our SF-MWCNT-PdNi$_{mix}$ (335.3 eV) is comparable to the binding energy value (335.4 eV) recently reported for PdNi alloy supported on MWCNT [32], suggesting that our ultrasonic-mixing technique formed an alloy. Also observed in the XPS of SF-MWCNT-PdNi$_{mix}$ is the occurrence of Pd in oxide forms. In addition, figure 4b shows the detailed spectrum of Ni 2p peaks which shows a prominent peak at ~ 854 eV which is an indication that the Ni is in an oxide form. From the shape of the spectrum, it is evident that more than one type of oxo-nickel species (i.e., Ni$_x$O$_y$, NiOOH, etc) may be present.

3.3   Electrochemical characterization

3.3.1 Electrode response in KOH solution alone

The cyclic voltametric evolutions of GCE-modified MWCNT-Pd, MWCNT-PdNi$_{mix}$ and MWCNT-PdSn$_{mix}$ conducted in 0.5 M KOH (Figure 5) gave the expected signatures of hydrogen adsorption/desorption peaks (in the −0.6 and −1.0 V region) as well as the prominent palladium oxide reduction process at ~ −0.33 V. The electrochemically-active surface area (EASA) was estimated from the PdO reduction peak. The SF-MWCNT-PdSn$_{mix}$ (63.58 m^{2}g^{-1})

gave higher value than the SF-MWCNT-PdNi$_{mix}$ (58.82 m^{2}g^{-1}) and SF-MWCNT-Pd (60.44 m^{2}g^{-1}) catalysts, meaning that Sn has more influence on the EASA of the Pd.

3.3.2 The effect of carbon supports and metal alloys on the electrocatalytic oxidation of ethanol

Figure 6 exemplifies typical cyclic voltammetric evolutions of ethanol oxidation (in 0.5 M KOH + 0.5 M C$_2$H$_5$OH) at the alloyed PdSn nanoparticles supported at three different carbon supports (Vulcan XC-72, AF-MWCNTs and SF-MWCNTs). The results indicate that the sulfonated MWCNTs give the best current response compared to the commercially available Vulcan XC-72 or the carboxylated MWCNTs. Thus, all subsequent studies were devoted to the metal catalysts supported on the SF-MWCNTs.

Next, we investigated the impact of using the bimetallic mixture (SF-MWCNT-PdM$_{mix}$) or alloy (SF-MWCNT-PdM) on the electrocatalytic oxidation of ethanol. As exemplified in Figure 7, the bimetallic mixture (SF-MWCNT-PdSn$_{mix}$) exhibits the most pronounced enhancement towards ethanol oxidation than the alloyed SF-MWCNT-PdSn electrocatalyst, implying that alloying impedes ethanol oxidation presumably due to the inhibition of the ethanol adsorption/dehydrogenation process on Pd. A mixture ratio of 1:1 (Pd : M) was used as it gave the best current response. The reason for this behaviour of the 'mixture catalysts' is not fully

understood at this moment, however, the following may be argued. First, MWCNTs are long entangled concentric tubes, each tube interacting with the adjacent tubes via strong π-π bonds. Such interaction could lead to the formation of some single-layer carbon supports. It may not be completely ruled out that the treatment adopted in the formation of our catalyst 'mixtures' and modification of electrode (i.e., longer period of ultrasonication, assisted by Nafion cross-linkages followed by heating) could encourage the separate catalysts sitting in different MWCNT supports to be close enough to form alloy as suggested by the XPS data. Second, the Sn or Ni species could possibly dissolve from the mixed catalysts during treatment process and redeposit on / near the Pd sites thus giving a catalyst structure similar to those described by Long et al [32]. This is corroborated by both the XPS and the XRD patterns that suggest the formation of alloy. Third, XPS data clearly prove the presence of the oxygenated species (oxides and hydroxides) of the Pd, Ni and Sn. It is well established that higher content of oxygenated species enhance the catalytic activities compared to their pure metal alloys [33-35]. For example, according to Bambagioni *et al* [35], the beneficial effect of the Ni on the Pd systems for ethanol oxidation in alkaline medium has been associated with the oxophilicity of the Ni to generate the Ni-OH moieties. Based on this finding, all subsequent experiments were devoted to the use of mixtures rather than the alloyed bimetals.

Note that the voltammetric curves obtained here are characteristic of ethanol oxidation in alkaline media at Pd-based electrodes. The mechanism of ethanol oxidation is still a subject of some controversy [1, 36,37], as it involves intermediate products (such as linearly adsorbed CO and CO_2, $CHx_{,ads}$ species [38-43] and final products (such as CO_2, acetaldehyde and acetic acid [42,43]) However, from recent reports [1,40] on Pd and Pd/Ti based ethanol oxidation in alkaline, the simplified mechanistic steps may be represented as follows:

$$CH_3CH_2OH \longleftrightarrow (CH_3CH_2OH)_{ads} \tag{1}$$

$$(CH_3CH_2OH)_{ads} + 3\,OH^- \longrightarrow CH_3CO_{ads} + 3H_2O + 3e^- \tag{2}$$

$$OH^- \longleftrightarrow OH^-_{ads} + e^- \tag{3}$$

$$CH_3CO_{ads} + OH^-_{ads} \longrightarrow CH_3COOH \tag{4}$$

$$CH_3COOH + OH^- \longrightarrow CH_3COO^- + H_2O \tag{5}$$
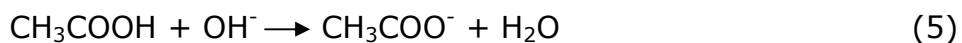
Equation 1 and 2 describe the dissociative adsorption of ethanol on the catalyst surface. Equation 4 represents the rate-determining step, meaning that the degree of ethanol oxidation is dependent on the coverage of the CH_3CO_{ads} and OH_{ads} on the surface of the catalyst.

3.3.3 Comparative electrocatalytic oxidation of ethanol

Figure 8a shows the comparative cyclic voltammetric responses of ethanol oxidation at GCE modified with SF-MWCNT-Pd, SF-MWCNT-PdNi$_{mix}$ and SF-MWCNT-PdSn$_{mix}$. The data show that the activity of

the SF-MWCNT-Pd is significantly increased on addition of Ni or Sn nanocatalyst. The ratio of the forward anodic peak current density (I_f) to the reverse anodic peak current density (I_b) i.e (I_f/I_b) is indicative of the ability of the catalyst to tolerate the accumulation of carbonaceous species [44-46]. Thus, low I_f/I_b ratio indicates poor oxidation of ethanol during the forward anodic scan; high I_f/I_b ratio suggests the converse. The electrode with Pd alone (SF-MWCNT-Pd) gave poorer I_f/I_b ratio and current density than the bimetallic catalysts. The PdSn$_{mix}$ system showed broader peak compared to the SF-MWCNT-Pd or SF-MWCNT-PdNi$_{mix}$, presumably due to the involvement of more than one oxidation state of Sn, and/or the different locations of the Sn nanoparticles at the different environments of the SF-MWCNTs leading to different but very close oxidation potentials of the ethanol. As should be expected, Figure 8b proves that pure SF-MWCNT-Sn and SF-MWCNT-Ni exhibited no activity towards ethanol compared to the SF-MWCNT-Pd.

The onset potential for ethanol oxidation is the same for the three electrocatalysts. However, when compared with other electrocatalytic parameters (current density and the I_f/I_b ratio) summarised in Table 1, the SF-MWCNT-PdSn$_{mix}$ is the most favoured catalyst system. The SF-MWCNT-PdSn$_{mix}$ system gave the highest peak potential ($E_p \approx 0.25$ V), meaning sluggish kinetics for ethanol oxidation compared to the SF-MWCNT-PdNi$_{mix}$ and SF-MWCNT-Pd. However, of major interest is the observation that the

current peak density on both SF-MWCNT-PdSn$_{mix}$ and SF-MWCNT-PdSNi$_{mix}$ systems is much higher than that observed at the SF-MWCNT-Pd, meaning that the Pd-M$_{mix}$ systems are more active than the Pd alone. Increased amount of OH$_{ads}$ on the catalyst surface (due to oxophilicity of the Ni and Sn to generate the Sn-OH or Ni-OH moieties) is believed to favour the formation of the acetate (CH$_3$COO$^-$) by coupling with CH$_3$CO$_{ads}$. Other researchers have also observed the beneficial effect of the Ni on the Pd catalyst [35,47,48].

Table 1: Comparative electrochemical performances of ethanol oxidation on GCE-SF-MWCNT-Pd, GCE-SF-MWCNT-PdSn$_{mix}$ and GCE-SF-MWCNT-PdNi$_{mix}$ nanocomposites measured in a 0.5 M ethanol + 0.5 M KOH solution at a sweep rate of 50 mVs^{-1} (n = 9).

Electrocatalyst	Electrocatalytic performance data			
	J_f / mA cm^{-2}	E_{onset} / V	E_p / V	I_f/I_b
SF-MWCNT-Pd	35.2±0.02	-0.50±0.02	-0.07±0.02	0.90
SF-MWCNT-PdNi$_{mix}$	67.2±0.02	-0.50±0.02	0.08±0.02	1.24
SF-MWCNT-PdSn$_{mix}$	68.7±0.02	-0.50±0.02	0.24±0.02	1.27

Figure 9a compares the linear sweep voltammograms at a sweep rate of 1 mVs^{-1} at the three electrodes in 0.5 M C$_2$H$_5$OH + 0.5 M KOH aqueous solutions. Figure 9b shows the plots of η vs. log$i$ (from the quasi-steady state curves in Fig. 9a), giving Tafel slopes

of 180 mV dec^{-1} (GCE-SF-MWCNT-PdNi$_{mix}$), 211 mV dec^{-1} (GCE-SF-MWCNT-PdSn$_{mix}$) and 209 mV dec^{-1} (GCE-SF-MWCNT-Pd). The value of $\alpha n \approx 0.3$ for all the electrodes, the n = 3 for ethanol oxidation [38,40]. Thus $\alpha \approx 0.1$, indicative of the irreversibility of the ethanol oxidation process [40]. The Tafel data also suggest that similar reaction mechanism is probably operating at the three electrodes. Tafel slopes higher than 118 mV dec^{-1} as obtained here are characteristic of porous electrode with high internal surface area leading to high electrocatalytic activities [49]. Charge transfer control region is very narrow on such electrodes and mass transport interferences cannot be totally ignored.

3.3.4 Stability studies: Chrono-analysis

Chronopotentiometric experiments were performed to provide further insights into stability of each of the electrodes. Figure 10 shows the chronopotentiometric curves of ethanol oxidation on the three electrodes at 3 mAcm^{-2}. The ethanol oxidation on the SF-MWCNT-PdNi$_{mix}$ occurred at low potential ($\sim$ 0.6 V) with minor potential oscillation while the oxidation at the SF-MWCNT-Pd and SF-MWCNT-PdSn$_{mix}$ occurred at higher potential (2.0 – 2.5 V) with significant potential oscillations. Higher potential polarizations accompanied by oscillations are indicative of poor catalysis and / or poisoned electrocatalyst [50]. Thus, this result clearly suggests that at the conditions employed in this work, the tendency for the

electrocatalytic sites of the catalysts to be blocked by the adsorbed species during ethanol oxidation increases as SF-MWCNT-PdNi$_{mix}$ << SF-MWCNT-PdSn$_{mix}$ < SF-MWCNT-Pd. Considering the poor activity of the SF-MWCNT-Pd electrode, all subsequent studies were devoted to the SF-MWCNT-PdNi$_{mix}$ and SF-MWCNT-PdSn$_{mix}$ based electrodes.

3.3.5 Effect of carbon monoxide on ethanol oxidation

Adsorption of carbon monoxide (CO) or CO-like species on the surface of the electrocatalyst is used to evaluate the extent to which an electrocatalyst can tolerate poisoning in a fuel cell system [46,51]. Figure 11 compares the effect of CO on the direct oxidation of ethanol in alkaline medium at the SF-MWCNT-PdNi$_{mix}$ and SF-MWCNT-PdSn$_{mix}$ electrodes. At the SF-MWCNT-PdNi$_{mix}$ electrode, the onset potential for ethanol oxidation in the presence of saturated CO is more positive (−0.27 V) than in the absence of saturated CO (−0.46 V). Similarly, at the SF-MWCNT-PdSn$_{mix}$ electrode, the onset potential in the presence of saturated CO (−0.46 V) is more positive than in the absence of it (−0.66 V). In both cases, the magnitude of potential shift is essentially the same (i.e., 200 mV), suggesting the same level of tolerance of CO. Both electrodes show similar current density ($\sim$ 13 mAcm^{-2}) upon interaction with CO, indicating a slightly better performance of the SF-MWCNT-PdNi$_{mix}$ than the SF-MWCNT-PdSn$_{mix}$ electrode.

3.3.6 Electrochemical impedance analysis

Electrochemical impedance spectroscopy (EIS) is a sensitive technique for determining the heterogeneous electron transfer kinetics [52-55], as well as the electrocatalytic oxidation kinetics of small organic molecules in fuel cells [44-46]. Figures 12 exemplifies typical Nyquist plots obtained at the GCE-SF-MWCNT-PdNi$_{mix}$ and GCE-SF-MWCNT-PdSn$_{mix}$ in 0.5 M C$_2$H$_5$OH + 0.5 M KOH. The spectra were satisfactorily fitted with the $R_s(R_{ct}CPE)$ circuit where R_s is the electrolyte resistance, R_{ct} is the charge transfer resistance, while *CPE* is the constant phase element. The impedance data are summarised in Table 2, simply indicating that the charge transfer resistance is higher at the SF-MWCNT-PdSn$_{mix}$ than at the SF-MWCNT-PdNi$_{mix}$ electrode towards ethanol oxidation. The observed slow kinetics at the SF-MWCNT-PdSn$_{mix}$ will likely lead to the build-up of ethanol reaction intermediates that would inhibit further adsorption of ethanol on the electrode surface.

Table 2: Comparison of the electrochemical impedance data for the GCE-modified SF-MWCNT-PdSn$_{mix}$ and SF-MWCNT-PdNi$_{mix}$ in a 0.5 M methanol + 0.5 M KOH solution at a sweep rate of 50 mVs^{-1} biased at two different potentials.

Bias / V	Electrochemical impedance parameter			
	R_s / Ω	R_{ct} / $k\Omega$	n	CPE/ mF
	GCE-SF-MWCNT-PdNi$_{mix}$			
0.20	64.6±0.7	2.6±0.1	0.9±0.1	0.7±0.1
0.30	64.6±0.5	2.1±0.1	0.9±0.1	0.9±0.1
	GCE-SF-MWCNT-PdSn$_{mix}$			
0.20	83.2±1.1	5.9±0.5	0.9±0.1	2.1±0.1
0.30	87.4±0.8	2.6±0.1	1.1±0.1	2.3±0.1

3.3.7 *Impact of varying the concentrations of ethanol or KOH on the voltammetric behaviour*

Figure 13 shows the linear sweep voltammetric (LSV) evolutions of different concentrations of ethanol (0.50 – 3.0 M range) in 0.5 M KOH at the SF-MWCNT-PdNi$_{mix}$ and SF-MWCNT-PdSn$_{mix}$ electrodes at a sweep rate of 1 mV s^{-1}. At both electrodes, the current density increased in proportion with the ethanol concentrations until at 1.5 M (for the SF-MWCNT-PdNi$_{mix}$) or 2.0 M (for the SF-MWCNT-PdSn$_{mix}$), where they stabilised and then decreased until 3.0 M: approximately from 7 mA cm^{-2} at 1.5 M to 6.5 mA cm^{-2} at 3.0 M for the SF-MWCNT-PdNi$_{mix}$; and from 21 mAcm^{-2} at 1.25 M to 16 mA cm^{-2} for the SF-MWCNT-PdSn$_{mix}$. The ethanol oxidation peak

potential shifted positively with increasing concentration (from -0.167 V at 0.5 M to -0.008 V at 3.0 M for the SF-MWCNT-PdNi$_{mix}$, and from -0.127 V at 0.5 M to 0.001 V at 3.0 M for the SF-MWCNT-PdSn$_{mix}$), indicating poorer electron transport process at the SF-MWCNT-PdSn$_{mix}$ than seen at the SF-MWCNT-PdNi$_{mix}$ electrode. The phenomenon of the oxidation peak shifting to more positive potentials at high ethanol concentrations may related to the mass transfer resistances or build-up of adsorbates formed during the electro-oxidation process or the combination of both [21,56]. This result corroborates the EIS data.

At high ethanol concentration, the electrocatalyst becomes easily saturated, presumably, as also proposed by others [40,56], due to the depletion of OH$_{ads}$ by CH$_3$CO$_{ads}$ at the electrode surface. Simply put, at low ethanol concentrations, the reactions are governed by the diffusion of ethanol due to excessive OH$^-$ ions, whereas at high concentration the reactions are governed by the diffusion of OH$^-$ ions due to excessive ethanol. The same behaviour was also observed with cyclic voltammetry. From the plots of η vs log i (Figure 13), the Tafel slopes were smaller (178 – 186 mV dec^{-1}) for the SF-MWCNT-PdNi$_{mix}$ than for the SF-MWCNT-PdSn$_{mix}$ (210–255 mVdec^{-1}) at all ethanol concentrations studied. Figure 14 shows the dependence of log i vs log $C_{ethanol}$ at various fixed potentials from a region where the quasi-steady state curves obey the Tafel equation. The reaction order of ethanol at SF-MWCNT-PdSn$_{mix}$ is

almost independent of potential, and slightly higher than observed at the SF-MWCNT-PdNi$_{mix}$ (Table 3). At higher potentials, the reaction order is approximately 0.8 for both electrodes.

Table 3: Reaction orders with respect to OH$^-$ and ethanol for GCE-modified SF-MWCNT-PdNi$_{mix}$ and SF-MWCNT-PdSn$_{mix}$ (RSD ~ 5 %).

Potential (mV) (vs. Ag|AgCl)	SF-MWCNT-PdNi$_{mix}$		SF-MWCNT-PdSn$_{mix}$	
	OH$^-$	EtOH	OH$^-$	EtOH
-500	0.46	0.57	0.80	0.74
-475	0.52	0.64	0.79	0.74
-450	0.50	0.70	0.76	0.75
-425	0.52	0.78	0.71	0.73
-400	0.49	0.83	0.67	0.75
-375	0.53	0.82	0.60	0.74
-350	0.54	0.84	0.57	0.75
-325	0.53	0.83	0.56	0.75
-300	0.47	0.83	0.55	0.75

Similarly, the impact of different concentrations of the electrolyte (0.5 to 3.0 M KOH) at constant concentration of ethanol was investigated at both electrodes using LSV and CV. At both electrodes, the peak current increased with increasing KOH concentration until at 1.25 M, where it started to decrease until 3.0 M. The ethanol oxidation peak potential shifted negatively with increasing KOH concentration, indicating that the electrocatalytic oxidation kinetics of ethanol are enhanced by the greater availability

of the OH^- ions in the reaction solution, and hence a higher OH^- coverage on the electrode surface. From the plots of η vs log i, the Tafel slopes ranged between 185 and 210 mV dec^{-1} for the SF-MWCNT-PdNi$_{mix}$ and 165 − 212 mV dec^{-1} for SF-MWCNT-PdSn$_{mix}$ at all KOH concentrations studied. From the plots of the log i vs log C_{KOH} at various low fixed potentials, the reaction order of OH- is approximately 0.5 for the SF-MWCNT-PdNi$_{mix}$ and 0.8 for the SF-MWCNT-PdSn$_{mix}$. The SF-MWCNT-PdSn$_{mix}$ gave a reaction order of about 0.8 at low potential (− 500 to −450 mV), and ~ 0.6 − 0.7 at higher potentials (− 450 to −300 mV). The reaction order of ethanol at SF-MWCNT-PdNi$_{mix}$ is independent of fixed potential. The higher reaction order at the SF-MWCNT-PdSn$_{mix}$ with respect to the OH^- species may suggest the higher ability of the Sn compared to the Ni to generate OH^-_{ads} species which promote the oxidative removal of the adsorbed intermediates at the electrode surface.

3   Conclusions

Fast microwave-assisted solvothermal preparation of metal nanoparticles (Pd, Ni, Sn) supported on sulfonated multi-walled carbon nanotubes (SF-MWCNTs) has been described. The adopted synthetic process is fast, simple, efficient, and yield agglomerated metal nanoparticles on SF-MWCNTs. Electrocatalytic behavior of the MWCNT-Pd and its mixtures (i.e., SF-MWCNT-PdSn$_{mix}$ and SF-MWCNT-PdNi$_{mix}$) towards ethanol oxidation in alkaline medium was

investigated. The SF-MWCNT-PdNi$_{mix}$ platform gave better electrocatalytic performance towards ethanol oxidation compared to its SF-MWCNT-PdSn$_{mix}$ counterpart. It is proved that the PdM nanocomposite mixtures are more efficient electrocatalysts than their bimetallic nanoalloys for ethanol oxidation. Indeed, this work has shown the electrocatalytic properties of microwave-synthesised Pd-based bimetallic catalysts for potential usage in direct ethanol alkaline fuel cell technology.

Acknowledgements

References

1. Liang, Z.X.; Zhao, T.S.; Xu, J.B.; Zhu, L.D. *Electrochim. Acta* 2009, **54***,* 2203.

2. E. Antolini , E.R Gonzalez , *J. Power Sources* 2010, **195***,* 3431.

3. S. Guo, S. Dong, E. Wang, *Energy Environ. Sci.* 2010, **3**, 1307.

4. C. Bianchini, P.K. Shen, *Chem. Rev.* 2009, **109***,* 4183.

5. C. E. Banks, T. J. Davis, G. G. Wildgoose, R. G. Compton, *Chem. Commun.* 2005, 842.

6. K.I. Ozoemena, J. Pillay, and T. Nyokong, *Electrochem. Commun*., 2006, **8**, 1391*.*

7. K.I. Ozoemena, J. Pillay, Electrochim. Acta 2007, **52**, 3630.

8. K.I. Ozoemena, D. Nkosi, J. Pillay, Electrochim. Acta 2008, **53**, 2844.

9. V. Bambagioni, C. Bianchini, A. Marchionni, J. Filippi, F. Vizza, J. Teddy, P. Serp, M. Zhiani, *J. Power Sources* 2009, **190***,* 241.

10. W. Zhang, P. Sherrell, A.I. Minett, J.M. Razal, J. Chen, *Energy Environ. Sci.* 2010, **3**, 1286.

11. D. Nkosi, J. Pillay, K.I. Ozoemena, K. Nouneh and Munetaka Oyama, *Phys. Chem. Chem. Phys*., 2010, **12**, 604.

12. Y. Lee, S. Han, K. Park, *Electrochem. Commun.* 2009, **11***,* 1968.

13. C. Xu, L. Cheng, P. Shen, Y. Liu, *Electrochem. Commun.* 2007, **9***,* 997.

14. F. Hu, G. Cui, Z. Wei, P.K. Shen, *Electrochem. Commun.* 2008, *10,* 1303.

15. H. Meng, F. Xie, P.K. Shen, *ECS Trans.* 2006, *1,* 1-9.

16. M. Nie, H. Tang, Z. Wei, S.P. Jiang, P.K. Shen, *Electrochem. Commun.* 2007, *9,* 2375.

17. H.T. Zheng, Y. Li, S. Chen, P.K. Shen, *J. Power Sources* 2006, *163,* 371.

18. F. Hu, F. Ding, S. Song, P.K. Shen, *J. Power Sources* 2006, *163,* 415.

19. B.J. Landi, M.J. Ganter, C.D. Cress, R.A. DiLeo, R.P. Raffaelle, *Energy Environ. Sci.* 2009, *2*, 638.

20. A.T. Chidembo, K.I. Ozoemena, B.O. Agboola, V. Gupta, G.G. Wildgoose, and R.G. Compton, *Energy Environ. Sci.*, 2010, *3*, 228.

21. S.A. Mamuru, K.I. Ozoemena, T. Fukuda, N. Kobayashi, *J. Mater. Chem.* 2010, DOI:10.1016/j.elecom.2010.08.028.

22. J. Liu, A.G. Rinzler, H. Dai, J.H. Hafner, R. Kelley Bradley, P.J. Boal, A. Lu, and R.E. Smalley, *Science*, 1998, *280*, 1253.

23. M.P. Siswana, K.I. Ozoemena, T. Nyokong, *Electrochim. Acta* 2006, *52,* 114.

24. C.Y. Du, T.S. Zhao, Z.X. Liang, *J. Power Sources* 2008, *176,* 9.

25. Z. Sun, X. Zhang, Y. Liang, H. Li, *J. Power Sources* 2009, *191,* 366.

26. W. X. Chen, J. Y. Lee, Z. Liu, *Chem. Commun*. 2002, **8**, 2588

27. G. Garnweitner, M. Niederberger, *J. Mater. Chem*. 2008, **18**, 1171.

28. A. Sarkar, A. Vadivel Murugan, and A. Manthiram, *Fuel Cells* 2010, **10**, 375.

29. X. Li, W. Chen, J. Zhao, W. Xing, Z.Xu, *Carbon* 2005, **43**, 2168.

30. A. Vadivel Murugan, A.K. Viswanath, V. Ravi, B.A. Kakade, V. Saaminathan, *Appl. Phys. Lett.* 2006, **89**, 123120.

31. J. Zhao, W. Chen, Y. Zheng, X. Li, Z. Xu, *J. Mater. Sci.* 2006, **41**, 5514.

32. R. Li, Z. Wei, T. Huang, A. Yu, Electrochimica Acta, 2011, **56** 6860.

33. J.W. Long, R.M. Stroud, K.E. Swider-Lyons, D.R. Rolison, *J. Phys. Chem. B* 2000, **104**, 9772.

34. S.S. Gupta, S. Singh, J. Datta, *Mater. Chem. Phys.* 2009, **116**, 223.

35. V. Bambagioni, C. Bianchini, J. Filippi, W. Oberhauser, A. Marchionni, F. Vizza, R. Psarso, L. Sordelli, M.L. Foresti, M. Innocenti, *ChemSusChem*. 2009, **2**, 99.

36. Q. He, W. Chen, S. Mukerjee, S. Chen, F. *J.* Laufek, *Power Sources* 2009, **187**, 298.

37. W. Zhou, Z. Zhou, S. Song, W. Li, G. Sun, P. Tsiakaras, Q. Xin, *Appl. Catalysis B: Environmental* 2003, **46**, 273.

38. A.V. Tripkovic, K.Dj. Popovic, J.D. Momcilvic, D.M. Drazic, *J. Electroanal. Chem.* 1996, ***418***, 9.

39. H. Wang, Z. Jusys, R.J. Behm, *J. Power Sources* 2006, ***154****,* 351.

40. J. Liu, J. Ye, C. Xu, S.P. Jiang, Y.Tong, *Electrochem. Commun.* 2007, ***9****,* 2334.

41. V. Rao, Hariyanto; C. Cremers, U. Stimming, *Fuel Cells* 2007, ***7****,* 417.

42. R.B. de Lima, H. Varela, *Gold Bulletin* 2008, ***41****,* 15.

43. S.C.S. Lai, S.E.F. Kleyn, V. Rosca, M.T.M. Koper, *J. Phys. Chem. C.* 2008, ***112****,* 19080.

44. Z. Liu, L. Hong, *J. Appl. Electrochem.* 2007, 37, 505

45. W. Chen, J. Kim, S. Sun, S. Chen, *Langmuir* 2007, ***23***, 11303.

46. N.W. Maxakato, K.I. Ozoemena, C.J. Arendse, *Electroanalysis* 2010, ***22***, 519.

47. P.K. Shen, C. Xu, *Electrochem. Commun*. 2006, ***8***, 184

48. C. Xu, Z. Tian, P. Shen, S.P. Jiang, Electrochim. Acta 2008, ***53***, 2610.

49. J.N. Soderberg, A.C. Co, A.H.C. Sirk, V.I. Birss, J. Phys. Chem. B. 2006, ***110***, 10401.

50. F. Hu, C. Chen, Z. Wang, G. Wei, P.K. Shen, *Electrochim. Acta* 2006, ***52****,* 1087.

51. A. N. Gavrilov, E. R. Savinova, P. A. Simonov, V. I. Zaikovskii, S. V. Cherepanova, G. A. Tsirlina, V. N. Parmon, *Phys. Chem. Chem. Phys.* 2007, **9**, 5476.

52. M. E. Orazem, B. Tribollet, Electrochemical Impedance Spectroscopy, Wiley, Hoboken, NJ 2008, ch. 16.

53. N.S. Mathebula, J. Pillay, G. Toschi, J. A Verschoor, and K.I Ozoemena, *Chem. Commun*., 2009, **23**, 3345.

54. J. Pillay, K.I. Ozoemena, R.T. Tshikhudo and R.M. Moutloali, *Langmuir*, 2010, **26**, 9061.

55. K.I. Ozoemena, N.S. Mathebula, J. Pillay, and G. Toschi, *Phys. Chem*. *Chem. Phys.,* 2010, **12**, 345.

56. S.S. Gupta, J. Datta, J. Power Sources 2005, **145**, 124.

Scheme and Figure Captions

Scheme 1: Schematic of the preparation SF-MWCNT-M (M = Pd, Ni or Sn) nanocoposites using microwave-assisted strategy.

Figure 1: Comparative XRD patterns of (a) SF-MWCNT-Pd (i), SF-MWCNT-Ni (ii) and SF-MWCNT-PdNi$_{mix}$(iii), and (b) SF-MWCNT-Pd (i), SF-MWCNT-Sn (ii), and SF-MWCNT-PdSn$_{mix}$ (iii).

Figure 2: Typical TEM images of the (a) SF-MWCNT (inset is the pristine MWCNT prior to functionalization), (b) SF-MWCNT-Pd, (c) SF-MWCNT-Ni, and (d) SF-MWCNT-Sn nanocomposites.

Figure 3: Typical EDX spectra of the (a) SF-MWCNT-Pd, (b) SF-MWCNT-Sn, and (c) SF-MWCNT-Ni nanocomposites.

Figure 4: Typical X-ray photoelectron spectrum of SF-MWCNT-PdNi$_{mix}$ showing the spectrum of the Pd 3d energy peaks, and (b) the Ni 2p energy peaks.

Figure 5: Cyclic voltammograms of GCE-SF-MWCNT-Pd, GCE-SF-MWCNT-PdSn$_{mix}$, and GCE-SF-MWCNT-PdNi$_{mix}$ nanocomposites (at the fourth cycle) in 0.5M KOH solution. Scan rate: 50mV s^{-1}.

Figure 6: Comparative cyclic voltammograms obtained in 0.5M KOH + 0.5 M C$_2$H$_5$OH solutions using GCE modified with alloyed PdSn nanocatalyst supported on various carbon materials, Vulcan XC-72, AF-MWCNTs and SF-MWCNTs. Scan rate: 50 mV s^{-1}.

Figure 7: Comparative cyclic voltammograms obtained in 0.5M KOH + 0.5 M C_2H_5OH solutions using GCE-SF-MWCNT-PdSn$_{mix}$ and GCE-SF-MWCNT-PdSn. Scan rate: 50 mV s^{-1}.

Figure 8: Comparative cyclic voltammograms obtained in 0.5M KOH + 0.5 M C_2H_5OH solutions for (a) SF-MWCNT-Pd, GCE-SF-MWCNT-PdSn$_{mix}$ and GCE-SF-MWCNT-PdNi$_{mix}$, and (b) SF-MWCNT-Pd, SF-MWCNT-Sn and SF-MWCNT-Ni. Scan rate: 50 mV s^{-1}.

Figure 9: A quasi-steady-state curve (1 mVs^{-1}) of the ethanol oxidation on the Pd/S-MWCNTS, PdNi/S-MWCNTs and PdSn/S-MWCNTs electrocatalysts in 0.5 M C_2H_5OH + 0.5 M KOH aqueous solutions. The Tafel plot of the ethanol oxidation on the Pd-S-MWCNTS, PdNi-MWCNTs and PdSn-S-MWCNTs electrocatalysts in 0.5 M C_2H_5OH + 0.5 M KOH aqueous solutions.

Figure 10: Chronopontetiometric curves of of GCE-SF-MWCNT-Pd, GCE-SF-MWCNT-PdSn$_{mix}$ and GCE-SF-MWCNT-PdNi$_{mix}$ in 0.5 M C_2H_5OH + 0.5 M KOH aqueous solutions at fixed current density of 3 mA cm^{-2}.

Figure 11: Comparison of the influence of CO on SF-MWCNT-PdNi$_{mix}$ and SF-MWCNT-PdSn$_{mix}$ electrodes in 0.5 M ethanol + 0.5 M KOH solution with or without the presence of saturated CO. Scan rate = 25 mVs^{-1}.

Figure 12: Nyquist plots obtained during the oxidation of ethanol oxidation at the different electrodes. The equivalent circuit shown was used in fitting the electrochemical impedance spectra, data summarised in Table 2.

Figure 13: Linear sweep voltammograms for ethanol oxidation reaction on the SF-MWCNT-PdNi$_{mix}$ and SF-MWCNT-PdSn$_{mix}$ modified GCE in 0.5 M KOH solution containing ethanol solutions of various concentrations. Scan rate = 1 mV s^{-1}.

Figure 14: The log-log plot of current density vs ethanol concentration in 0.5 M KOH obtained at different potentials on SF-MWCNT-PdNi$_{mix}$ and SF-MWCNT-PdSn$_{mix}$ modified GCE.
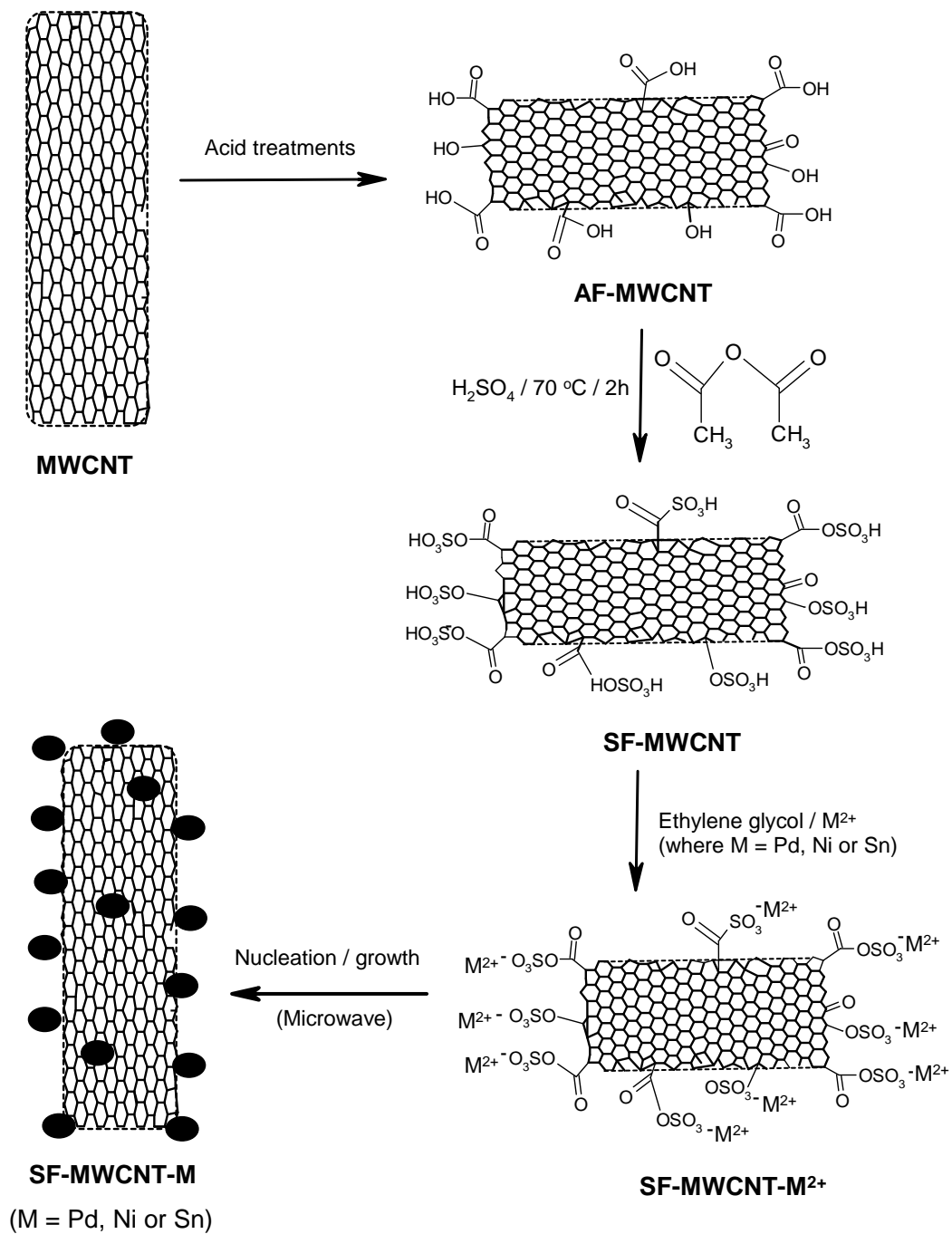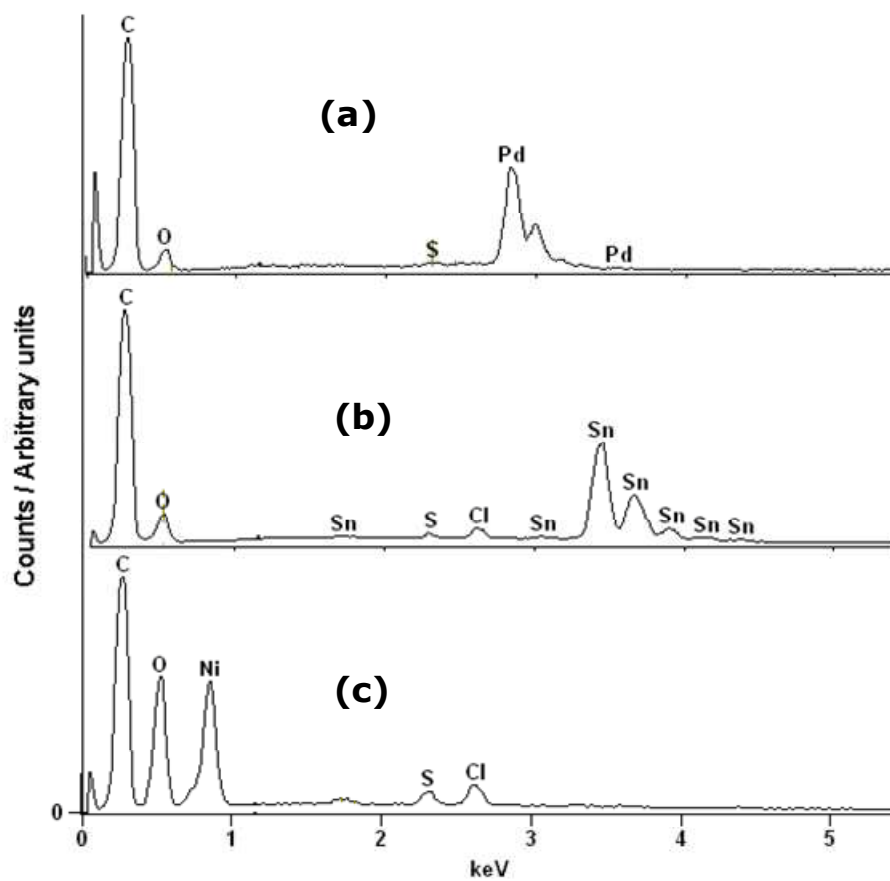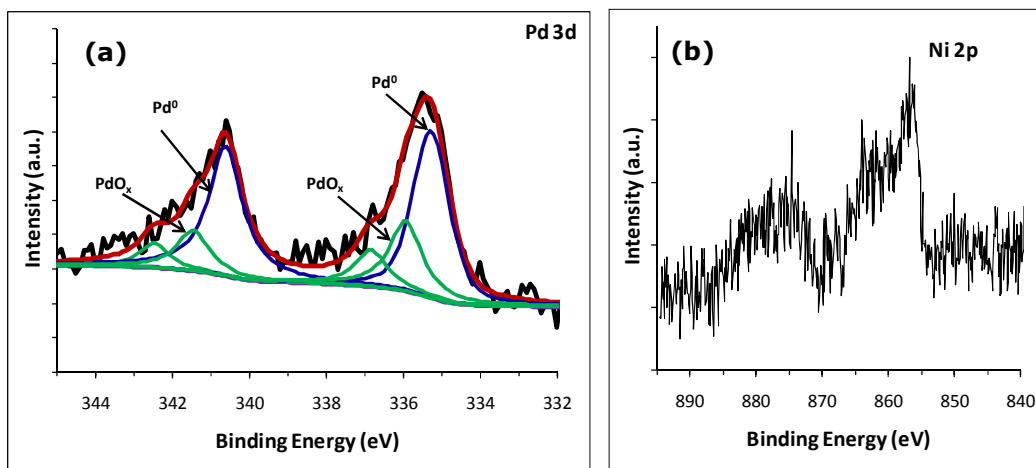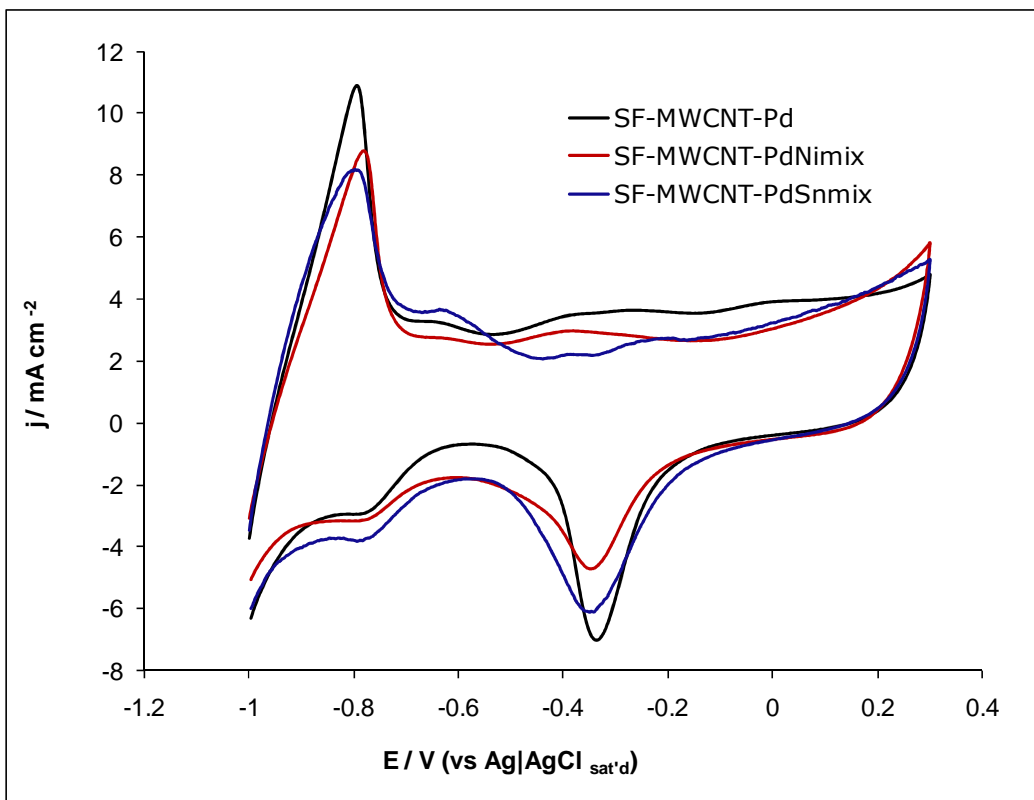
Scheme 1
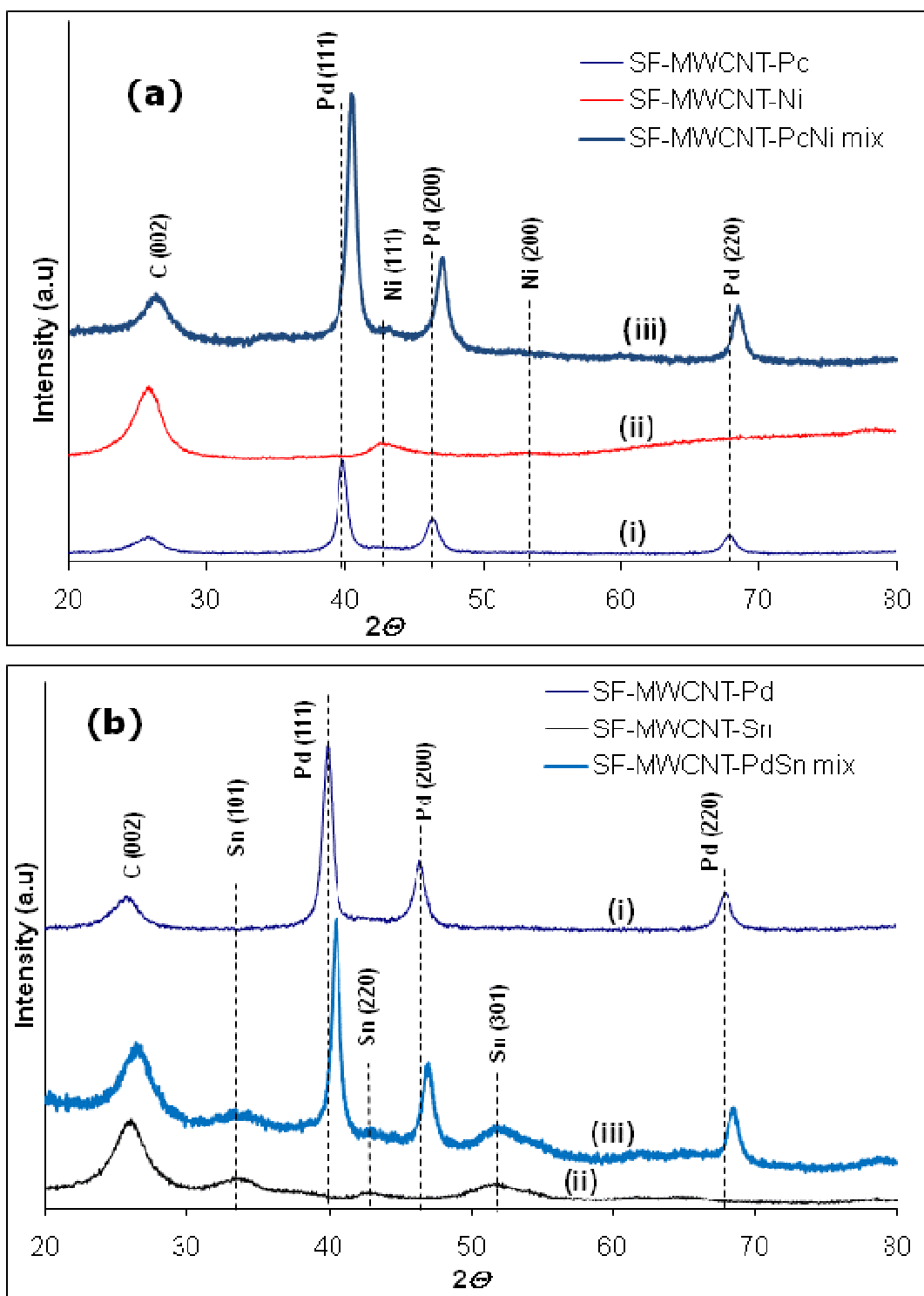
Figure 1
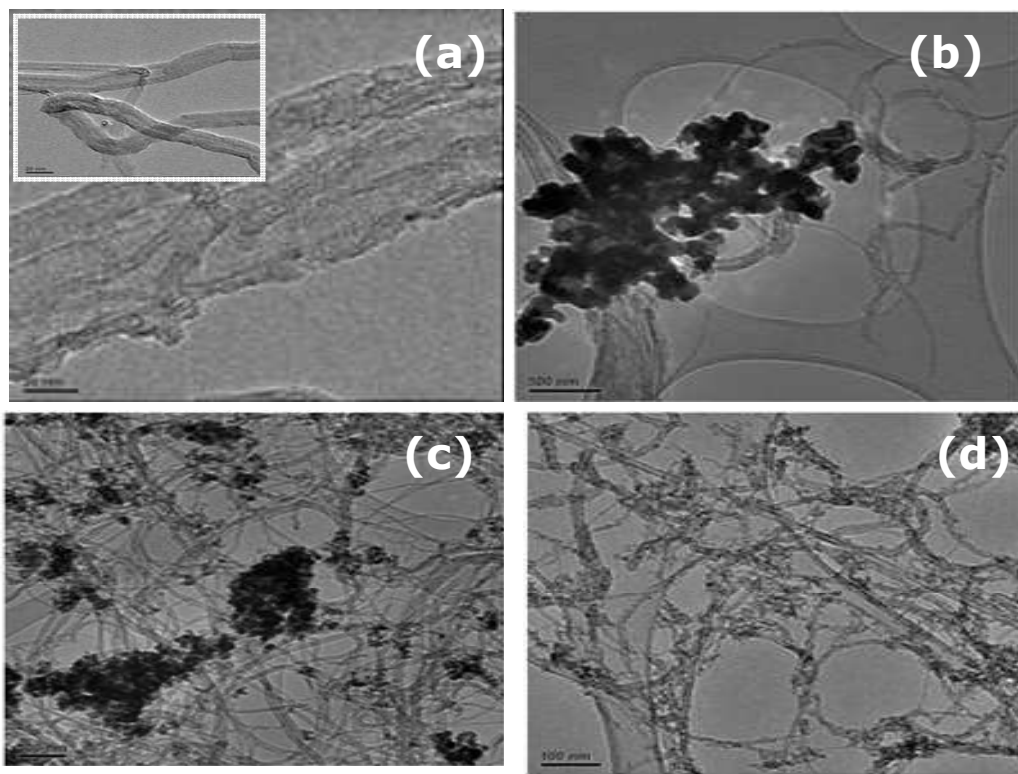
Figure 2

Figure 3

Figure 4

Figure 5
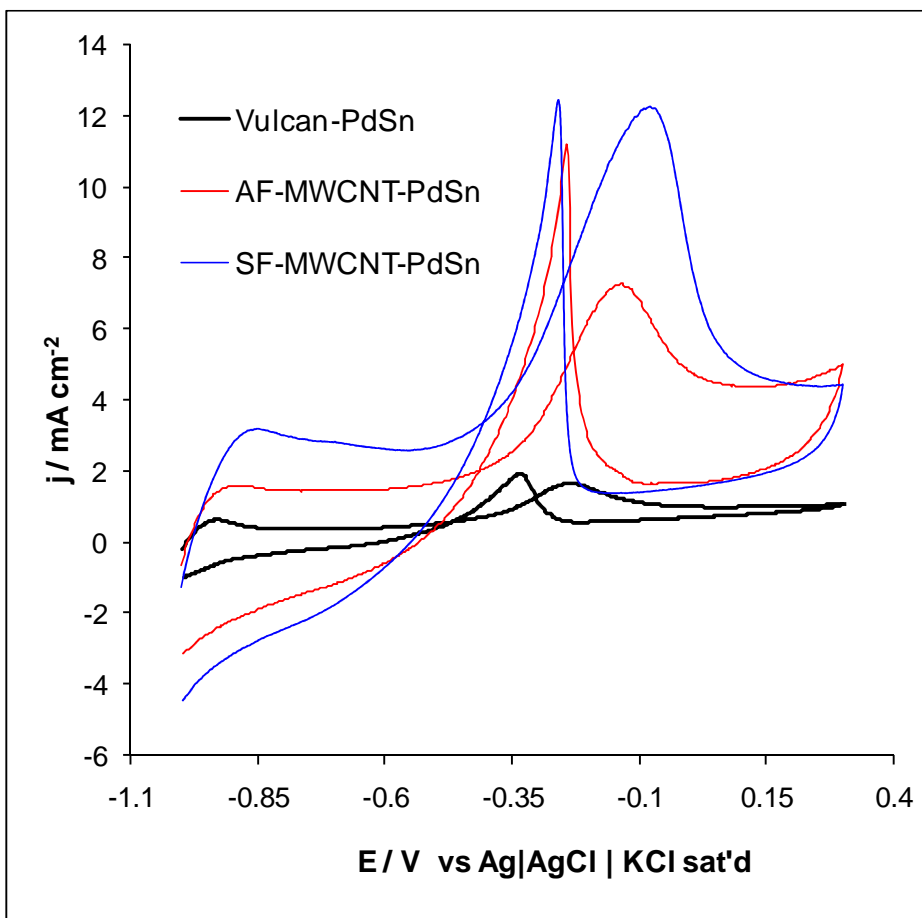
Figure 6
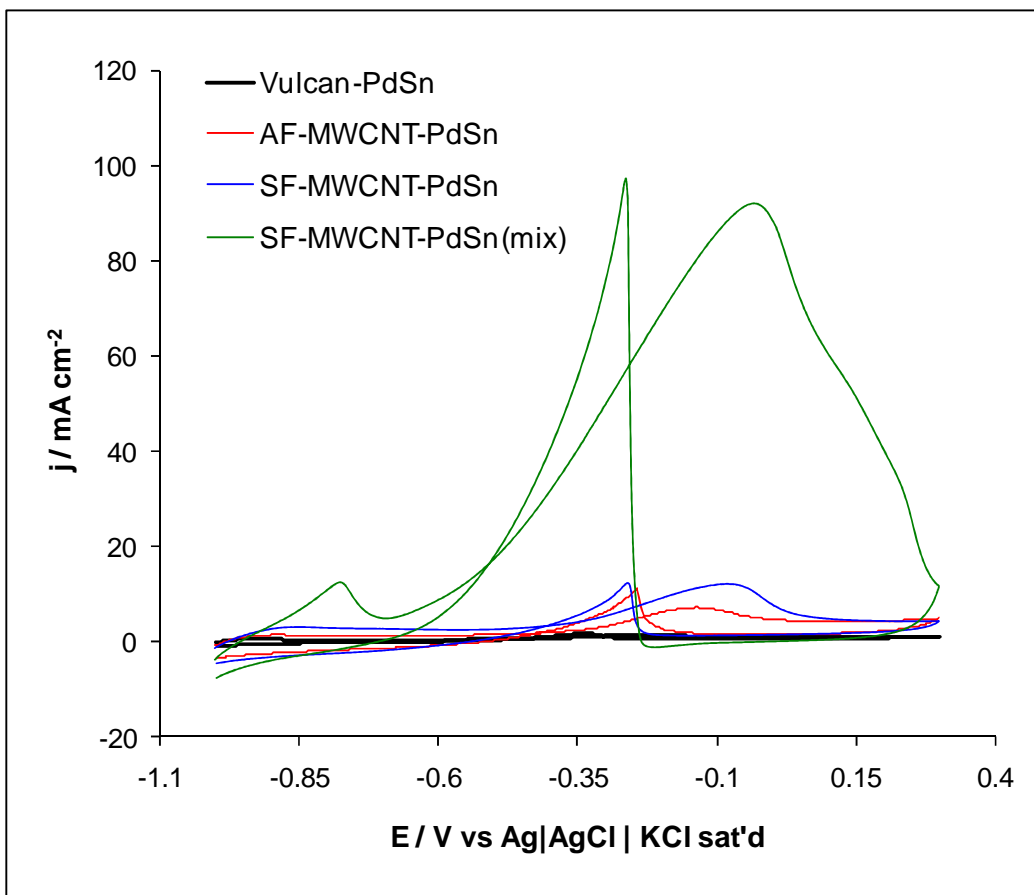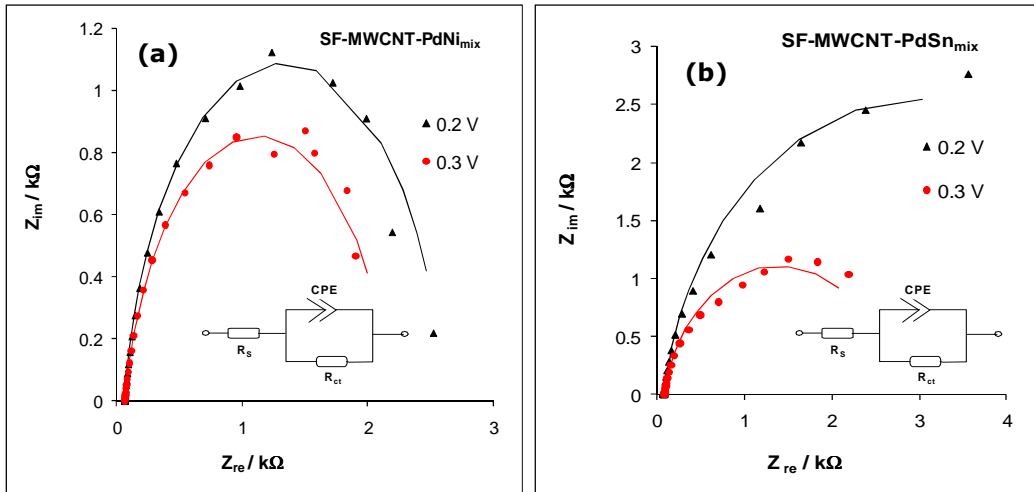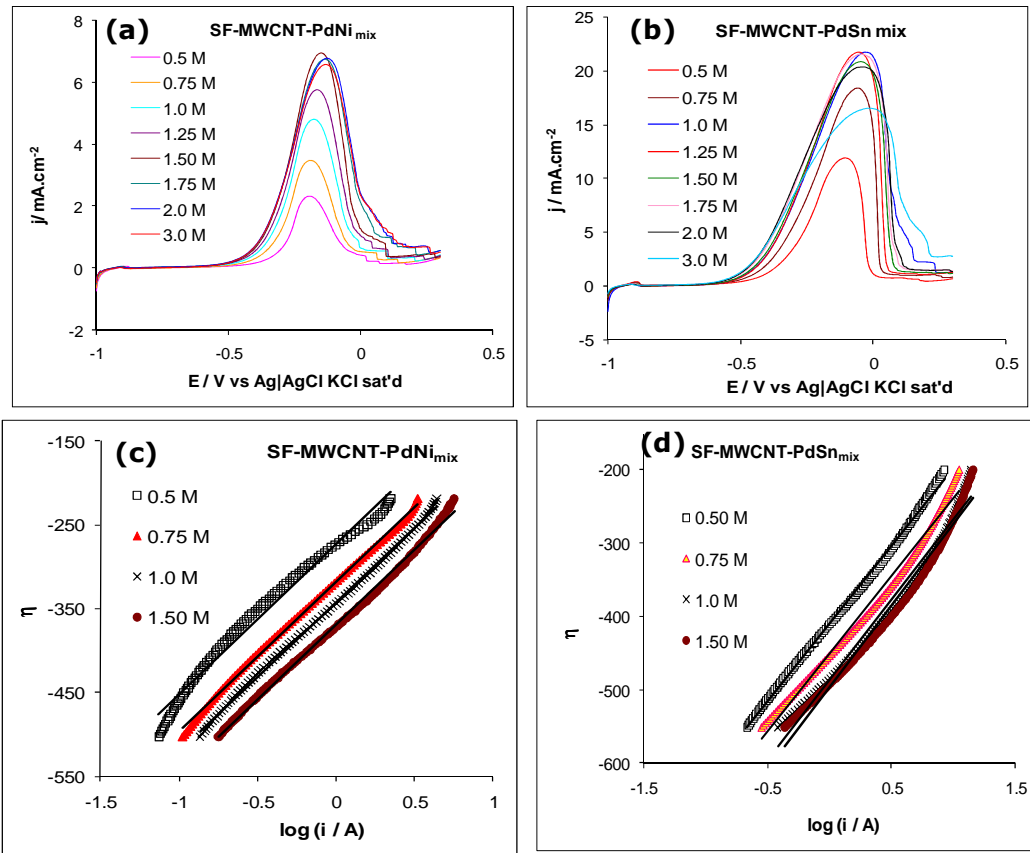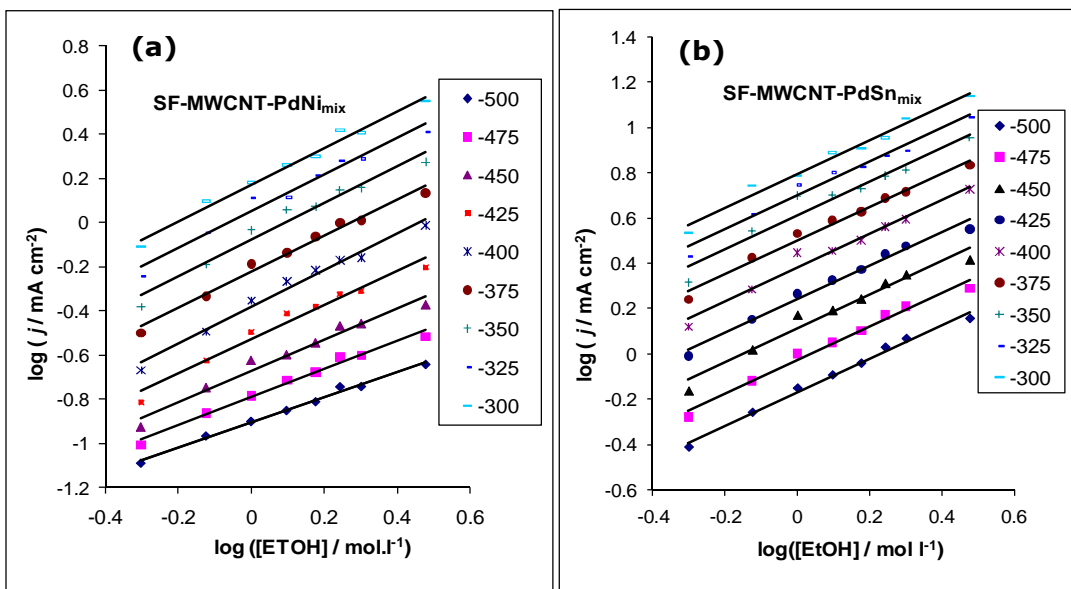
Figure 7
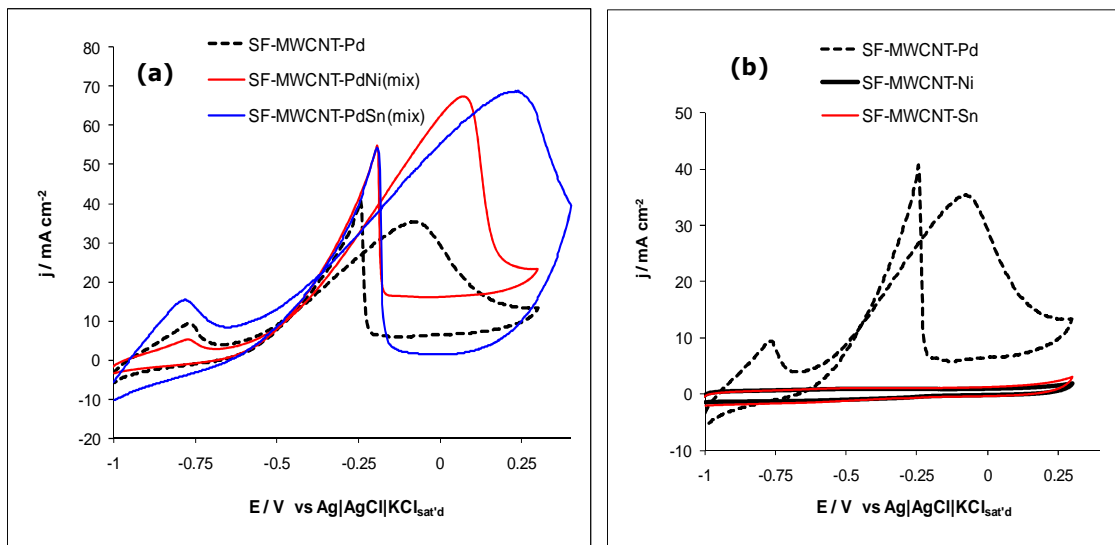
Figure 8
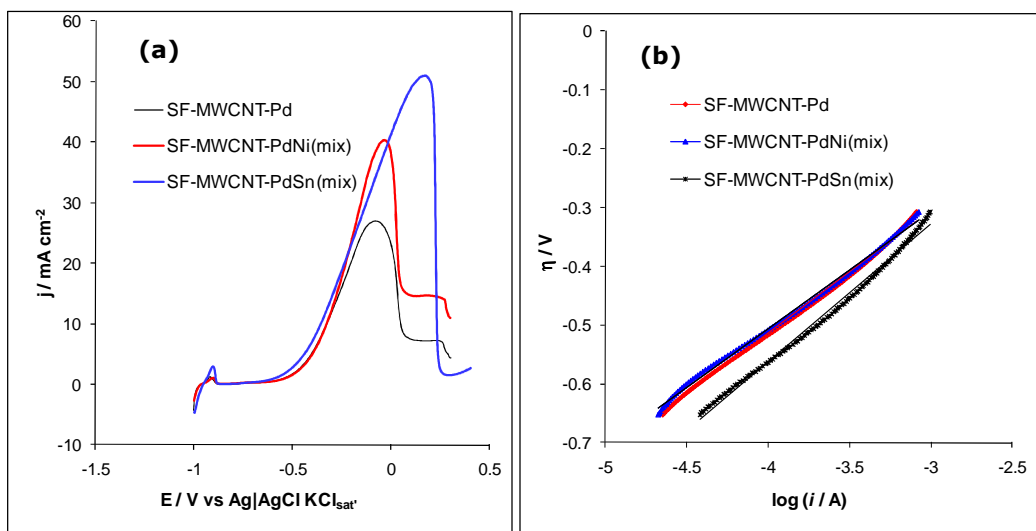
Figure 9
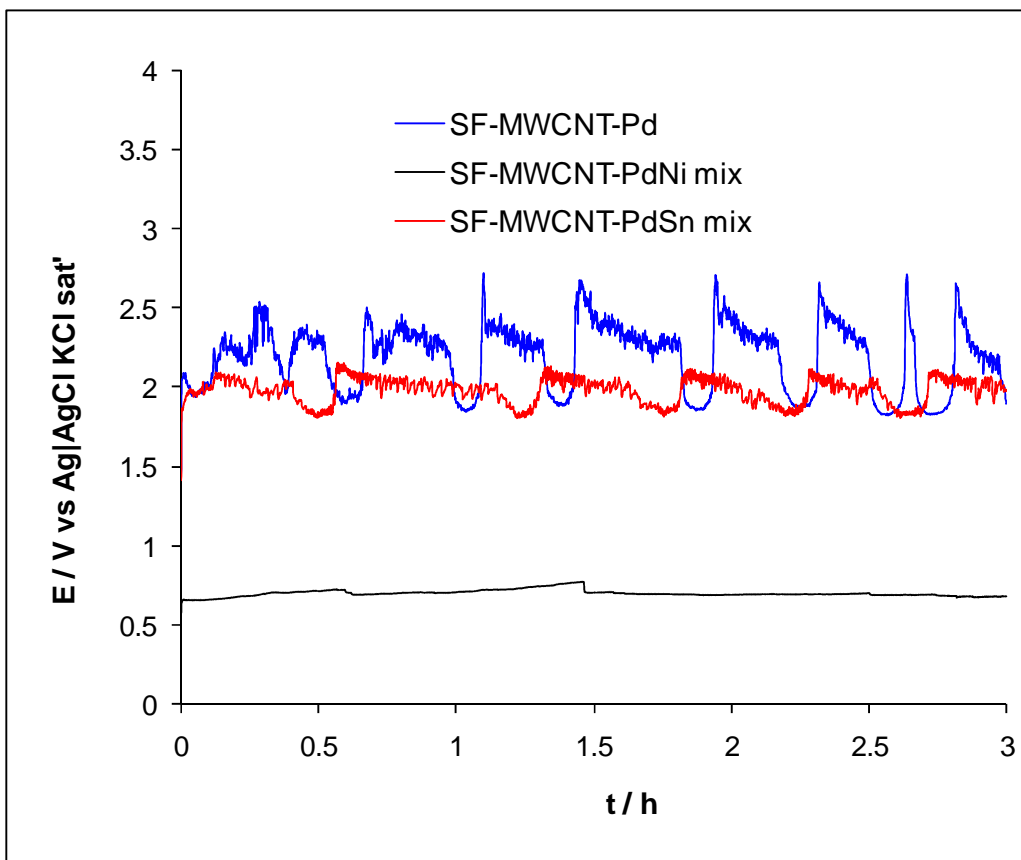
Figure 10
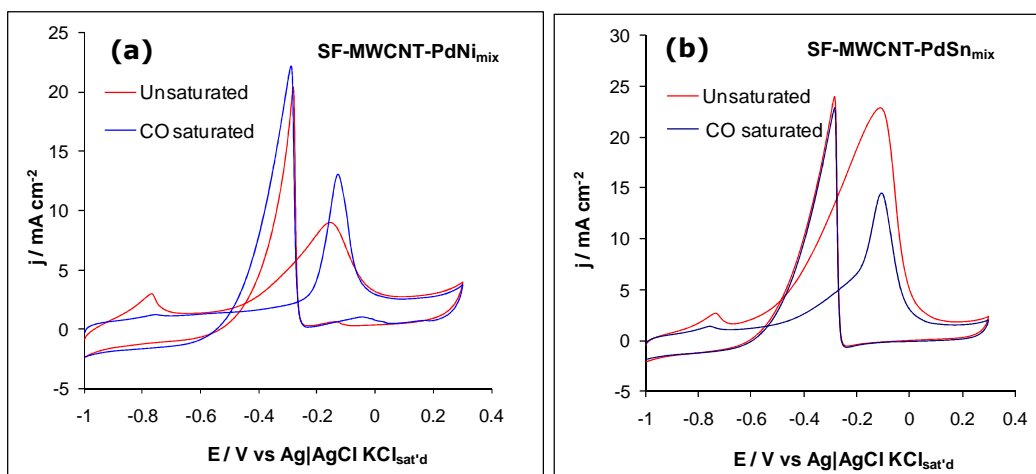
Figure 11

Figure 12

Figure 13

Figure 14